28. High-Energy Physics Applications of EGS[*]

A. Del Guerra[†] and Walter R. Nelson[‡]

Department of Physics, University of Pisa
Piazza Torricelli 2, I-56100, Pisa, Italy[†]

Stanford Linear Accelerator Center, Stanford University
Stanford, CA 94309[‡]

28.1 INTRODUCTION

When a shower takes place in a large detector mass, most of the incident energy appears as ionization or excitation in the medium. The energy of the initiating particle can be determined to a reasonable degree by sampling the energy deposited in the device—hence, the name "calorimeter". Calorimetry has become an essential tool for high-energy physics experiments. With the new colliders—*e.g.*, LEP and LHC at CERN, HERA at DESY, SLC at SLAC, and the proposed SSC in the U.S.— calorimeters have almost completely replaced conventional spectrometers for particle identification and the measurement of their energy. Furthermore, the particle physics concept of *jets* has shifted the instrumentation emphasis from individual particle measurement to precise determination of the energy balance of multiparticle systems—*i.e.*, towards *calorimetry*. Unfortunately, the complexity of these devices increases tremendously in the hundred-GeV energy range, and it is therefore important to have reliable simulation tools available for designing calorimeters and evaluating their performance with specific experiments in mind.

In this chapter, we will present the use of the EGS4 code[1] in electromagnetic calorimetry. After a short review of the physics of the electromagnetic cascade itself, and of the various types of shower counters that exploit it, several comparisons of EGS simulations with relevant experiments will be presented. As a specific example, the application of EGS4 to the design of a lead-glass drift calorimeter will be discussed. Finally, we will present a series of other applications of the EGS code in high-energy physics, including accelerator design, health physics, and radiation damage in general.

28.2   THE EGS CODE IN ELECTROMAGNETIC CALORIMETRY

28.2.1   The electromagnetic cascade shower.

When a high-energy electron or photon enters a material, it produces an electromagnetic (EM) shower with the following properties:

— The fraction of the energy, E, of the incident particle which is absorbed by the material is distributed among a large number of secondary particles; the thickness necessary for total absorption increases as $\ln E$.

— The entire shower is well collimated; hence, the shower axis is a fairly good representation of the direction of the incident particle.

— The inherent fluctuation in energy deposition of the shower, both in magnitude and in position, depends upon the material in which the shower develops, and limits intrinsically the energy resolution and the position determination.

To describe an EM shower, several quantities are of general use for every material:

- The *radiation length* X_0 (g/cm^2), given by[2]

$$X_0 = 716.4A[Z^2(\ln 184.2Z^{-1/3} - f) + Z\ln 1194Z^{-2/3}]^{-1} , \qquad (28.1)$$

where Z and A are the atomic number and weight, respectively, and f accounts for the Coulomb correction according to:

$$f = 1.202x - 1.0369x^2 + 1.008x^3/(1 + x) , \qquad (28.2)$$

with

$$x = (Z/137)^2. \qquad (28.3)$$

- The *photon absorption length*, λ (g/cm^2), given by

$$\lambda = 1/\mu \approx 9X_0/7 , \qquad (28.4)$$

where μ is the attenuation coefficient.

- The *Molière radius*, r_m (g/cm^2), which characterizes (or scales) the lateral spread of the shower, and is given by the approximate formula

$$r_m \approx \frac{21}{\epsilon}X_0 , \qquad (28.5)$$

where $\epsilon \approx 800/(Z + 1.2)$ is the *critical energy* (MeV)—*i.e.*, the energy at which the collision energy loss is equal to the bremsstrahlung loss.

Since EM shower development is built upon the repetition of a few physical processes, Monte Carlo simulation is well suited as an application tool. Among the many codes which have been implemented[3-7], the EGS4 code by Nelson, Hirayama, and Rogers[1] is now most widely used. However, while the detailed shower development is accurately described by the Monte Carlo tables and histograms, the gross features of

the cascade can be described by "phenomenological" parameters[8], such as the *median depth*, i.e., the depth within which one half of the energy is contained,

$$t_{med}(X_0) = \ln(E/\epsilon) + 1.22 \approx t_{max}(X_0) + 1.0 , \tag{28.6}$$

where $t_{max}(X_0)$ is the depth at which the shower reaches its maximum. The shower is 98% <u>longitudinally</u> contained for a length of $\sim 3t_{med}$, whereas it is 95% <u>laterally</u> contained for a size of 1.5 to $2r_m$[8].

28.2.2 Electromagnetic calorimeters.

Electromagnetic calorimeters can be subdivided into two main categories: *homogeneous* and *sampling* (see Fig. 28.1).
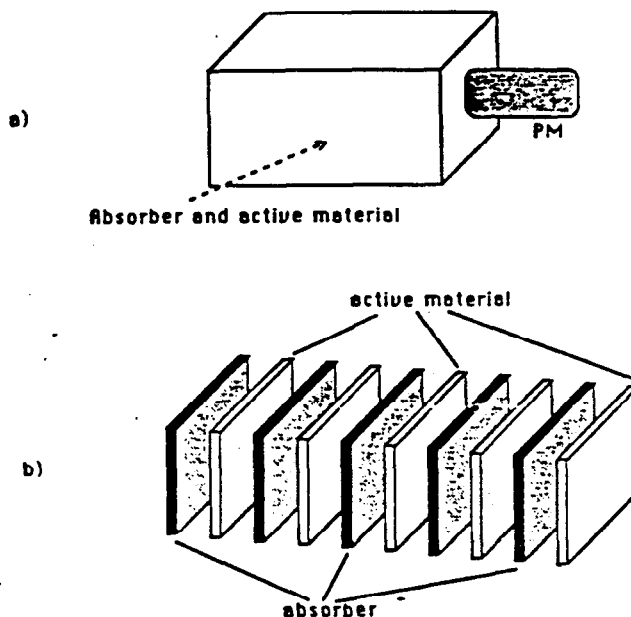

Figure 28.1. Schematic of: a) homogeneous calorimeter, b) sampling calorimeter.

In the first category, the absorbing block is also the active material in the detection process. Since all the energy lost by the shower is dissipated in the active material, in principle this type of detector gives the best energy resolution, limited only by the cutoff energy (i.e., the energy below which the detector is not responding), by the detector inhomogeneity, and by the *intrinsic* resolution of the detector. However, homogeneous calorimeters tend to be expensive, and their size often places limitations on the *spatial* resolution that can be obtained.

With sampling calorimeters, the cascade develops in a dense material, and the energy lost, is usually sampled in slices of active material interspaced between the absorbers (Fig. 28.1b). In this case, the detector is cheaper and its geometry is more flexible. If an adequate number of readout channels are used, the intrinsic spatial

resolution can be excellent. However, the energy resolution is degraded by the sampling fluctuations.

Homogeneous calorimeter.

Table 28.1 shows the main properties of the most common scintillators and the energy resolution, in the GeV range, obtained for homogeneous calorimeters[9]. At higher energies, the imperfections and the inhomogeneity of the larger fiducial volume for the shower dominate, and the energy resolution deteriorates.

Table 28.1. Properties of Most Common Scintillators and Intrinsic Energy Resolution for Homogeneous Calorimeters (E in GeV)[9].

Crystal	NaI(Tℓ)	BGO	Pb-Glass (SF-6)
Density (g/cm^3)	3.7	7.1	5.2
X_0 (cm)	2.59	1.12	1.69
$\sigma(E)/E$	$\sim 0.3\%/E^{1/2}$	$\sim 0.4\%/E^{1/2}$	$3.6\%/E^{1/2}$

NaI(Tℓ) is a standard scintillator, and its performance is well known[10]—it has a high scintillation efficiency (5 times larger than plastic scintillators), a short radiation length ($X_0 \sim 2.6$ cm), and a low cutoff energy. The main problems arise from the long decay time of its scintillation (230 ns for the fast component), which may cause pile-up problems. In addition, it is extremely hygroscopic and is not very resistent to radiation.

BGO is the most dense scintillator material and has the shortest radiation length ($X_0 = 1.12$ cm). More than 50% of its light is emitted within 60 ns, and it is very resistent to radiation. Unfortunately is quite expensive. Other crystals have been proposed (e.g., CsI(Tℓ) and BaF$_2$). BaF$_2$ scintillates in the UV region and needs a special readout, such as a gas detector doped with TMAE which absorbs UV light and produces photoelectrons[11]. Liquid argon and "warm" liquids have also been used as active materials.

Lead glass is a transparent glass containing PbO (50% to 70% by weight), with a typical radiation length of a few cm. In this case, the energy lost by the shower is measured by collecting the Cerenkov light produced by fast particles and transmitted through the glass. The energy resolution is mainly limited by the cutoff energy for light emission ($E_c \sim 0.5$ MeV). Although the resolution is not as good as for NaI(Tℓ), lead glass is superior in terms of cost, flexibility, and count rate capability.

Sampling calorimeter.

In a sampling calorimeter, the main contribution to the energy resolution comes from the sampling fluctuations. The energy deposited in the active part of a sampling calorimeter will fluctuate statistically, and the energy resolution will depend on the thickness of the absorber. It has been experimentally shown[8] that the energy resolution follows the general law of $E^{-1/2}$, with an additional dependence on the thickness, t (g/cm^2), of the absorber slab and on the critical energy, ε (MeV). Namely,

$$\frac{\sigma}{E} \propto \frac{\sqrt{\varepsilon} \cdot \sqrt{t}}{\sqrt{E}} , \tag{28.7}$$

where E is in GeV. This rough dependence has to be refined in real calorimeters[12]. Typical experimental values are[9] :

$$\frac{\sigma(E)}{E} = \frac{17\%\sqrt{t}}{\sqrt{E}} \quad \text{for scintillator or liquid argon,} \qquad (28.8)$$

$$\frac{\sigma(E)}{E} = \frac{25\%\sqrt{t}}{\sqrt{E}} \quad \text{for gaseous detector.} \qquad (28.9)$$

In a gaseous detector, the low density leads to an increase in the length of charged particle tracks. Together with an enhancement of Landau fluctuations, the net result is that energetic delta rays, traveling along the sampling gap, can deposit atypically large amounts of energy in a single cell. At very high energy, where σ/E becomes of the order of a few percent, the instrumental noise and the intercalibration become as important as the sampling resolution, or even the most significant contribution, as for homogenous calorimeters.

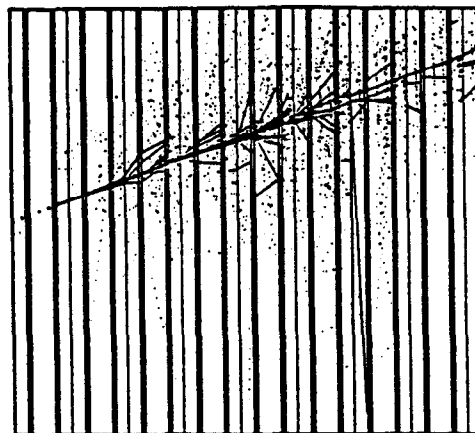### 28.2.3 EGS4 simulation of EM calorimeters in general.

As described in the manual[1], the user communicates with the EGS4 code by means of subroutines HOWFAR (to specify the geometry) and AUSGAB (to score and output the results). Initialization for these routines is done in MAIN.

For homogeneous calorimeters, the simulation is very simple because the geometry usually consists of a narrow beam impinging on a single block (Fig. 28.1a) of NaI, BGO, etc., and the scoring is done by keeping track of the total energy deposited in the active material (plus the lateral and longitudinal leakage if full containment is not achieved).

Sampling calorimeters are usually described by a series of absorbing slabs with active detector gaps interspaced to form what is commonly called a *sandwich counter*. The shower pictures shown in Fig. 28.2 and Fig. 28.3 represent a simulation* of the multi-wire proportional chamber (MWPC) array that was used in SLAC experiment E-137[13]. This shower calorimeter was made up of eight modules (see closeup Fig. 28.4), each consisting of:
- 8.9-cm air gap;
- Wire chamber (0.6-cm Al, 1.6-cm gas, 0.6-cm Al);
- 15.2-cm air gap;
- 1.0-cm plastic scintillator;
- 1.6-cm air gap;
- 8.3-cm aluminum converter, for detectors located in the (downbeam) modules (shaded in Fig. 28.3).

---

* The EGS4 User Code: UPE137.

55%

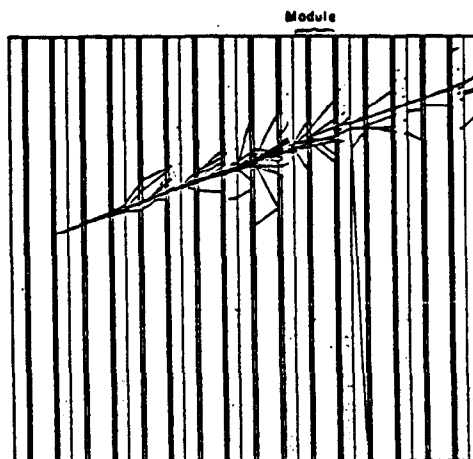Figure 28.2. Single 5-GeV photon entering at 20° (all particles shown).

Figure 28.3. Single 5-GeV photon entering at 20° (charged particles only).

Shower leakage (and other) fluctuations.
Both longitudinal and lateral shower leakage are clearly shown in Figs. 28.2-28.3. As stated earlier, fluctuations caused by shower leakage result in a decrease in the overall energy resolution of the calorimeter. Fluctuations can also be caused by charged particle tracks having lengths greater than the active detector gap width, such as those shown in the closeup view (Fig. 28.4) of one of the MWPC gas regions—identified in the figure as the region bounded on either side by a pair of the closest parallel planes. Of the 11 particles crossing the gap, the 9 in the middle traverse a gas distance slightly larger than the size of the gap itself (as a result of the 20° angle). However, the upper and lower tracks are 8 to 11 times longer, and the bottom one actually scatters back into the gas volume where it deposits even more energy. Pictures of this type aid in explaining how "channeling" within the detector gap—i.e., adding transverse absorbers around the wires in the gap to stop delta rays—can be an effective means of improving the overall energy resolution of sampling calorimeters.
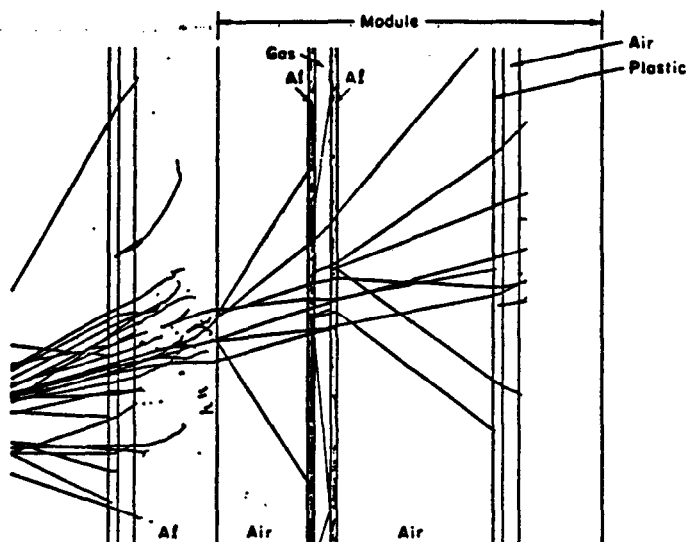
Figure 28.4. Expanded view of a portion of the previous figure, showing 11 charged particle tracks crossing a MWPC gas region (the wire chamber walls are shaded). The top and bottom particles travel much farther in the gas; the bottom one actually scatters back into it.

Detector response.

One of the most critical parameters in the simulation is the energy cutoffs—*i.e.*, the energy at which the radiation transport is terminated, and the remaining energy is deposited locally. Obviously, the photon and charged particle cutoffs should be set below the intrinsic energy response level of the detector if realistic simulations are to be made. A well known problem with EGS3, as a result of a 1-MeV (K.E.) cutoff limitation for charged particles, was the appearance of "ghostly" multipeaks in the energy distribution plots. With EGS4, this problem no longer exists since calculations can now be performed down to 10 keV.

Simulation efficiency.

EGS is primarily an *analog* Monte Carlo code—*i.e.*, each and every particle is followed to some completion throughout the simulation. With the release of EGS4, however, one is able to take advantage of various biasing and weighting schemes in order to speed up the simulation appreciably. In the case of EM calorimeter design, for example, a relatively simple Mortran3 macro[14] can be introduced at the beginning of the User Code in order to select preferentially the *leading particle* of an interaction—*i.e.*, the particle that has the highest energy. In other words, by biasing the calculation in favor of events that are the most significant to the development of the cascade, the overall efficiency increases. However, in order to "play the game fairly", some events must also be chosen randomly to represent the counterpart in the interaction. Furthermore, an appropriate weight factor must be assigned to each particle—to be carried along by the progeny—and any scoring must take the final particle weights into consideration (see the EGS4 manual[1] for a complete description of leading-particle biasing).

In Fig. 28.5, we have plotted the fraction of energy that leaks out of a gas sampling calorimeter as a function of the thickness. Somewhat simplier than the MWPC shown

in the previous figures, this semi-infinite sandwich counter consists of alternate layers of PbO (10 mm, $\rho = 6.2$ g/cm^3 (see Table 28.2)) and gas (1 mm at 10 atm). The solid curve represents a normal (*i.e.*, unbiased) EGS4 calculation and was obtained in six 20 minute runs at 10 GeV (8.62 sec/case). The closed circles were done using *leading-particle biasing* (0.031 sec/case), resulting in a factor of 277 increase in speed! Even though the agreement between the two is quite good, the error bars can further be reduced at large depths by allowing the leading-particle biasing to be applied only in the *important region*. That is, if we turn the scheme on during the initial 11 radiation lengths where 90% of the energy is deposited, and off for the remainder, we obtain the results shown as open circles (0.045 sec/case) in Fig. 28.5.
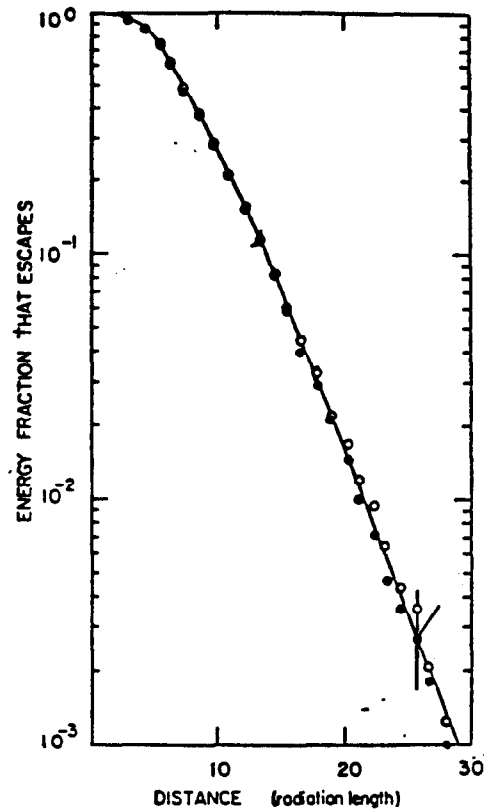

Figure 28.5. Longitudinal energy fraction leakage versus detector length for 10-GeV incident electron beam (solid curve: no biasing; closed circles: total biasing; open circles: limited biasing).

Efficiency in a Monte Carlo calculation can be measured by the inverse of the product of variance and calculation time (*e.g.*, see Chapter 18). In the present example, we have taken advantage of our "pre-knowledge" of the physics of EM cascades to select the most efficient calculation in determining the size of the calorimeter. To be specific, to determine the 99% shower containment depth of the calorimeter, it took about *two hours* of IBM-3081 computer time using the normal (unbiased) code, whereas the same results were obtained in about *two minutes* using limited leading-particle biasing.

Detector-resolution calculations.

One can use leading-particle biasing in order to save computer time when designing the overall size of a calorimeter—i.e., determining a predefined containment level to minimize fluctuations caused by leakage. However, importance sampling methods should not be used in resolution calculations themselves since the biasing and weighting will significantly distort the true statistical behavior. In other words, importance sampling can be exploited when determining a quantity involving the *average* behavior of a shower, but simulations involving event-by-event scoring must be done in an unbiased way. Although resolution calculations usually require lots of computer time, a calorimeter design method has been described by Hirayama et al.[15] in which most of the time-consuming calculations are done at the lower (faster) energies.

28.2.4 EGS4 design of a lead-glass drift calorimeter.

Principle of operation of a high-density time-projection calorimeter.

Drift-Collection Calorimeters[16] and High-Density Projection Chambers[17] have been proposed as a method of achieving fine granularity in gas sampling calorimeters while minimizing the number of readout channels. This is done by drifting the ionization produced in a gas-sampled radiator over a fairly large distance to a separate detecting wire plane. Digitization of the drift time allows the reading out of a complete "image" of the shower with a high degree of segmentation via a modest number of wires.

The construction schemes for these devices usually consist of plates of high-Z material alternating with gas sampling regions, with various drift field shaping arrangements. The field shaping arrangement is of great importance in avoiding loss of electrons while drifting in long narrow spaces, and numerous schemes have been proposed. EGS4 has been used extensively* to simulate a drift calorimeter[15] in which the radiator and drift field-shaping structures are combined in the form of high-density (~ 6 g/cm^3) lead-glass tubing[18]. A highly resistive layer of metallic lead, which acts as the continuous field shaping electrode, is formed by surface reduction of the lead oxide (Fig. 28.6). The tubes are fused together into a "honeycomb" structure with their axes perpendicular to the direction of the incident radiation. A prototype, consisting of lead-glass tubing of 40-cm drift length fused together to form a total longitudinal dimension of $\sim 20X_0$, has been constructed, and currently is being tested[19].

Simulating the honeycomb structure with a planar geometry.

Figure 28.7 is a schematic of the proposed calorimeter. For the Monte Carlo simulation, the tube geometry was approximated by alternating semi-infinite slabs of lead glass and gas regions, with the effective dimensions chosen so as to give the same average cross-sectional area of gas and solid material when viewed from the edge of the slabs (or tubes) (see appendix in Hirayama et al.[15]).
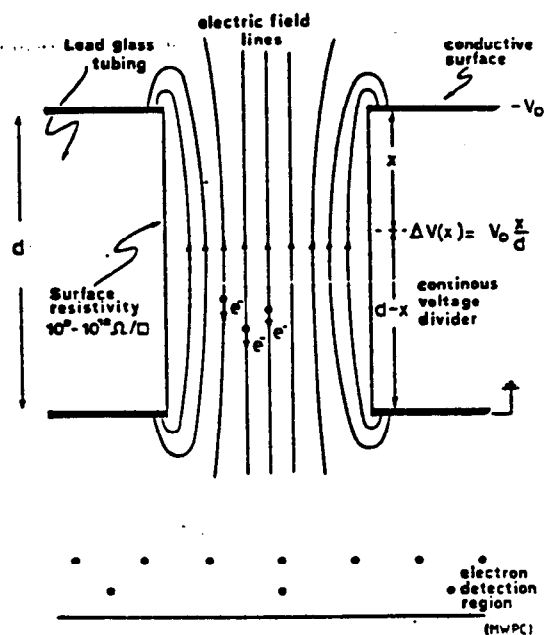
---

* The EGS4 User Code: UCCAL2DW.

Figure 28.6. Single element schematic of a high-density drift structure (*i.e.*, lead-glass tube) equipped with a conventional MWPC.
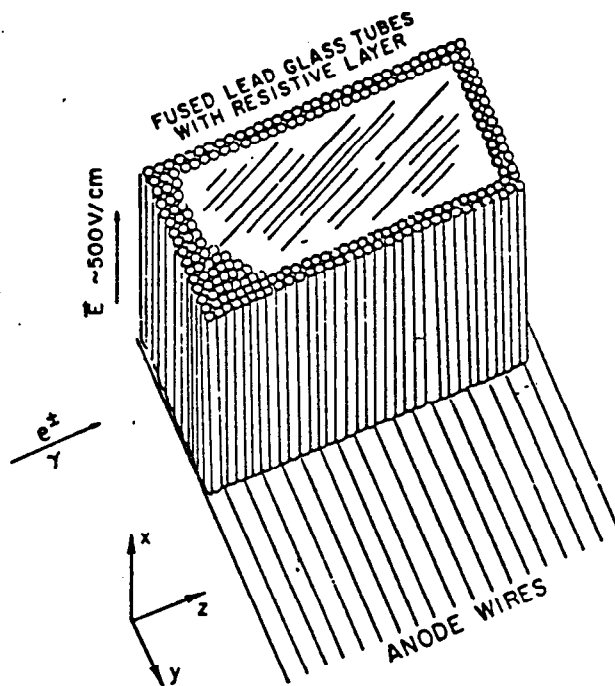

Figure 28.7. Overall schematic of the high-density drift calorimeter with lead-glass radiator (drift tube) structure and wire-chamber readout.

The track-length restriction that normally would be imposed by the tubes in the direction transverse to the tube axes was retained by appropriately limiting the energy deposition along the track. This was done in SUBROUTINE AUSGAB where, in addition, an algorithm was included in order to sample Landau fluctuations of the energy deposited in the gas by the charged particles. The effect of varying the inner diameter of the tube (i.e., the length of gas seen by the charged particles) is shown in Fig. 28.8 for the case of 1 GeV, for a gas pressure of 1 atmosphere, and for a total length of $15X_0$. The four curves correspond to the four combinations of applying (or not) the track length restriction and Landau sampling algorithms. The actual detector situation is given by the curve labeled "TR/Landau".
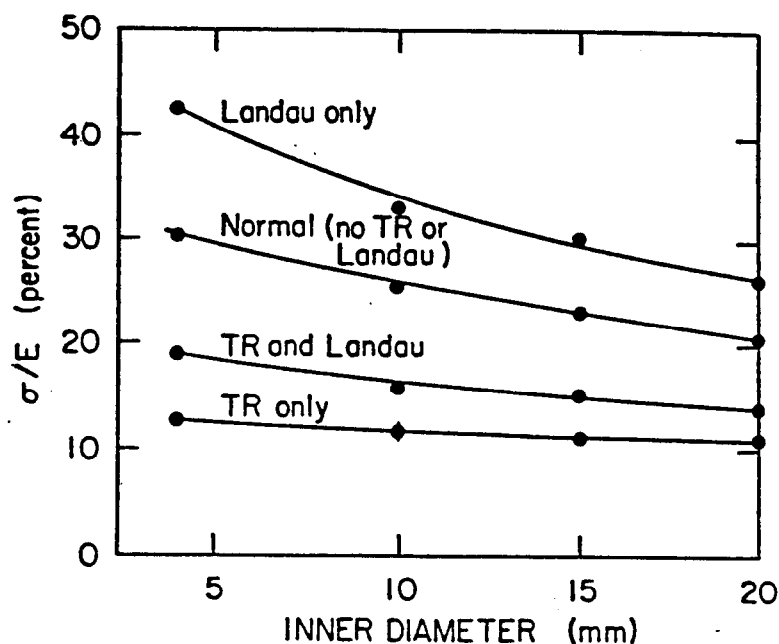

Figure 28.8. Fractional energy resolution as a function of the inner diameter of the tubes (1 GeV/$15X_0$/1 mm wall/1 atm.), for various combinations of track length restriction and Landau sampling.

Optimization of the design of the calorimeter.

The wire-plane readout for a drift collection calorimeter may be operated either in the standard *proportional* mode or in one of the modes in which the pulse is *saturated* (e.g., the *self-quenching streamer* mode[20]). In the former, the signal collected from each wire is proportional to the amount of energy deposited in the tubes sampled by that wire. The resolution of a calorimeter operating in this mode is degraded by the Landau fluctuations in the energy deposited by each track. In the *saturated* modes, one uses *digital sampling* in which the energy is assumed to be proportional to the number of tracks counted. This eliminates the deleterious effects of Landau fluctuations, but can cause the energy response of the calorimeter to saturate at high energies due to overlapping tracks being registered as a single particle traversing a calorimeter cell.

In order to model the two modes of operation, the Monte Carlo scoring was done in two ways. When the *proportional* mode was being simulated, the energy deposition in the gas regions was scored, and the width of the distribution gave the energy resolution

which would be achieved in an ideal (*i.e.*, no-electron-loss-during-drift) calorimeter, read out by an ideal proportional chamber. In simulating the *digital sampling* mode, the number of charged particles in the gas regions was scored. When more than one charged particle traversed a calorimeter cell, just one track was scored in order to mimic the effects of overlapping tracks at high energy.

Three tube geometries were studied with inner diameter/wall thicknesses of: 10/1, 5/1 and 5/2 mm. Each was filled with a gas mixture of 70% argon - 30% methane at pressures of 1, 2, 3, 5 and 10 atm. The 5/1 case was also examined with the gas filling replaced with liquid argon. These configurations were chosen to give reasonable drift efficiency, a modest number of readout channels, and a reasonably compact structure. In all cases, the simulated calorimeter was taken to be $20X_0$ in depth, and infinite in the transverse directions (x and y) to the beam direction (note: according to Fig. 28.5, $20X_0$ is sufficient for 99% shower confinement for incident energies up to 10 GeV[15]). Table 28.2 provides a summary of the characteristics of each configuration.

Table 28.2. Characteristics of Various Geometry Configurations Simulated.

	70% Argon - 30% Methane			Liquid Argon
Inner Diameter (mm)	10	5	5	5
Wall Thickness (mm)	1	1	2	1
Sampling Medium: ρ (g/cm^3)* X_0 (cm)*	0.00148P 14500/P	0.00148P 14500/P	0.00148P 14500/P	1.4 13.96
Radiator: ρ (g/cm^3) X_0 (cm)	6.2 1.28	6.2 1.28	6.2 1.28	6.2 1.28
Effective X_0 (cm)**	4.20	2.62	1.86	2.34
Sampling Thickness (cm)	X_0/4.5	X_0/4.8	X_0/2.6	X_0/4.4
Equivalent Average ρ (g/cm^3)	1.9	3.0	4.3	3.8

* P is the absolute pressure (atm.).
** Effective radiation length is the physical length of the device that is equivalent to one radiation length in the longitudinal shower development.

Figure 28.9 shows the fractional energy resolution (σ/E) at an incident electron energy of 1 Gev, as a function of gas pressure, for the three tube geometries. Results for both *proportional* and *digital* sampling are presented (solid lines drawn merely to guide the eye). The errors on these points were obtained by dividing the EGS runs, for each case, into five runs of approximately 200 incident showers each. Each data point and error bar correspond to the mean and standard deviation of the mean for the five runs for that case.
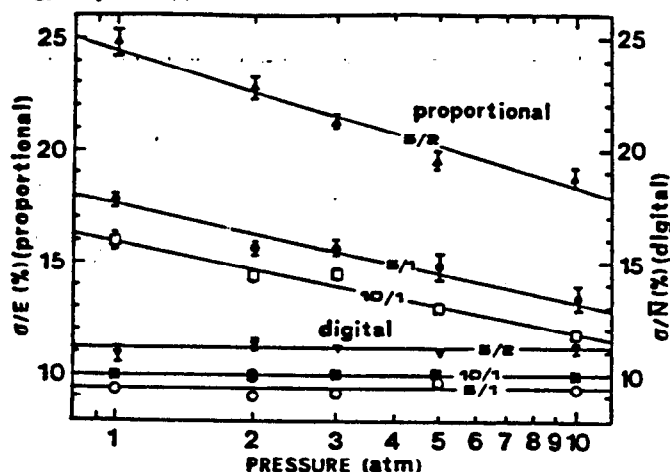
Figure 28.9. Fractional energy resolution at 1 GeV as a function of pressure for three tube geometries (both proportional and digital sampling).

In the *proportional* mode cases, the fractional resolution, as expected, shows improvement as the pressure is increased. This improvement is due to an effective increase in the amount of active gas region, which both diminishes the relative track fluctuations and causes a reduction in size of the Landau fluctuations.

The resolution achieved using *digital sampling* is clearly superior at this energy. The pressure independence of these resolution curves is a clear reflection of the effects of eliminating Landau fluctuations. The very good resolution given by digital sampling at 1 GeV makes this method an ideal choice for such applications as tracking calorimetry in nuclear-decay experiments. At higher energies the superiority of digital over proportional sampling begins to deteriorate as the effects of saturation become relevant.

We also modelled the response of the lead-glass tube structure filled with liquid argon. A fractional energy resolution of 5% at 1 GeV was predicted (5 mm diameter/1 mm wall), which is in good agreement with experimental results obtained by Hitlin[21] in finely sampled liquid argon calorimeters.

<u>Comparison with experimental results.</u>
In constructing the calorimeter, a glass different than that assumed in the calculations was used*. In order to have a compact calorimeter, tubes of 5 mm inner diameter, and 1 mm thickness were chosen (which also allowed for a reasonably long drift distance of 40 cm). Figure 28.10 shows the fractional energy resolution expected for this calorimeter as a function of pressure at 1 GeV for 20 radiation lengths, which implies full containment (i.e., 98-99%) of the shower. The energy dependence obtained from Monte Carlo simulation at 2 atm. was $\sigma/E \sim (14.8 \pm 0.3)\%/\sqrt{E}$. Preliminary experimental data[22] obtained on a 11.2 X_0 prototype at 2 atm. showed a σ/E of $(18 \pm 2)\%/\sqrt{E}$ in the energy range 2-5 GeV (Fig. 28.11). This experimental value is higher than the Monte Carlo prediction, and is probably due to longitudinal leakage. In fact, a Monte Carlo simulation of the 11.2 X_0 prototype response gives a value of $(16.2 \pm 0.6)\%/\sqrt{E}$ at 1 GeV and 2 atm., which compares fairly well with the experimental results.

---

* Schott RS-520, 71% PbO (by weight), $\rho = 5.2$ g/cm^3, $X_0 = 1.66$ cm.
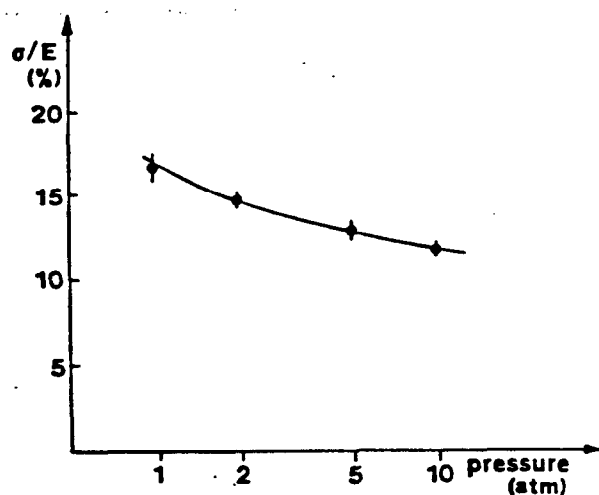
Figure 28.10. Fractional energy resolution at 1 GeV for a $20 - X_0$ calorimeter (currently being tested) operating in proportional mode, as a function of pressure. The solid line is drawn to guide the eye through the data.
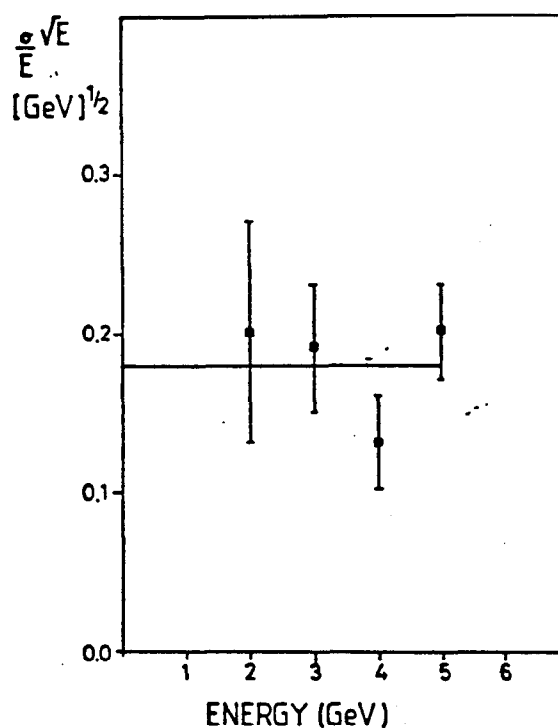
Figure 28.11. Energy resolution $(\sigma/\sqrt{E})$ as a function of the incident energy. Experimental data (with error bars) measured with a $11.2 - X_0$ prototype (solid line is a least-squares fit).

28.3 COUPLING EGS WITH HADRONIC CASCADE PROGRAMS

A subtantial fraction of the energy deposited in a hadron cascade is a direct result of EM cascades produced by the decay of π^0 mesons (mean life $\sim 10^{-16}$ sec) into two photons. EM showers, as we have discussed previously, are best measured <u>longitudinally</u> in terms of radiation length units, whereas the scale for the development of hadronic showers is given by the nuclear absorption (interaction) length λ_I (obtained from the inelastic cross section). Experimental values of λ_I for materials suitable for calorimetry of hadronic showers range from 12 cm (uranium) to 34 cm (carbon)[23]. The corresponding X_0 values are 0.32 cm (uranium) and 18.8 cm (carbon), so that the spatial distribution of the energy deposition along the direction of the beam is not really controlled by the EM cascade, but rather by the longitudinal development of the hadronic cascade itself.

We have also stated earlier that the <u>lateral</u> spread of EM cascades is conveniently measured in terms of the Molière radius, which is a manifestation of the dominant process involved—i.e., the multiple Coulomb scattering of low-energy electrons. The rms angle of multiple scattering is given approximately by

$$\theta \approx \frac{15\sqrt{t}}{p} \approx \frac{p_T}{p} , \qquad (28.10)$$

where the transverse and longitudinal momentum of the charged particle, p_T and p, respectively, are in MeV/c, and the distance, t, is in radiation lengths. However, since bremsstrahlung and pair production are the primary interaction processes involved in the development of the EM shower, one can let $t \approx 1$ and obtain

$$p_T(\text{EM}) \approx 15 \ (\text{MeV/c}) \qquad (28.11)$$

for the effective transverse momentum associated with EM cascades. The transverse momentum in hadron collisions, on the other hand, is determined, on average, by the "size" of hadrons, with the well known (for over 25 years) result[24]

$$p_T(\text{hadron}) \approx 350 \ (\text{MeV/c}). \qquad (28.12)$$

In other words, the lateral spread of energy deposition is also not controlled by the EM cascade, but by the hadron shower itself.

As a result of the above analysis, there is a large class of hadronic cascade problems that does not require a very sophisticated approach for handling the EM cascade component—e.g., target and dump heating, induced radioactivity, and even some hadron calorimetry studies. In these cases, a parameterization scheme can be employed to account for the EM shower, as has been done in the older versions of the FLUKA hadron cascade code. In the current versions of FLUKA[25,26], however, the user has the option to select a parameterization scheme for the EM cascade, or simply to couple EGS4 directly into the hadronic shower simulation[27].

28.3.1 Hadron calorimetry.

With the recent coupling of EGS4 with FLUKA87[25-27], one has the capability of running a hadron calorimetry problem in which the EM cascade part is done by EGS4. A

calorimetry "option" can be selected such that the built-in histogramming package produces plots for direct read-out of energy resolution. Furthermore, one can run a pure EM cascade—*i.e.*, one initiated solely by electrons or photons. As a result, the calorimetry ("signature") of photons (or electrons) and hadrons can be studied relative to one another using the built-in geometry package of FLUKA87, and thereby avoid any problems related to geometry/material normalization, etc.

EGS has also been used rather extensively for hadronic calorimetry in connection with the hadronic cascade code developed at the Oak Ridge National Laboratory called HETC[28]. A recent example of the use of EGS with HETC is provided in the study by Alsmiller *et al*[29].

28.3.2   Photohadron production with FLUKA87/EGS4.

Recently, the calculation of high-energy hadron cascades induced by electron and photon beams in the GeV energy range has been made possible[30] through the coupling of EGS4 with FLUKA87[25-27]. The most important source of high-energy hadrons around a multi-GeV electron accelerator is the hadronic interaction of real photons that are part of the EM cascade generated by the electron (or photon) beam. Using the EGS4 computer code, high-energy photons were allowed to interact hadronically according to the vector meson dominance (VMD) model, facilitated by a Monte Carlo version of the dual multistring fragmentation model (*i.e.*, "quarks") used in the FLUKA87 cascade code.

The results of this calculation compare very favorably with experimental data on hadron production in photon-proton collisions and, even more importantly, with data on hadron production by electron beams on extended targets—*i.e.*, with measured yields in secondary beam lines. In Fig. 28.12, a comparison is made between the coupled FLUKA87/EGS4 code and experimental data that was taken over 18 years ago when SLAC was first started up. The comparison is an absolute one, and the first of its kind!

This technique has already found use in the design of secondary beam lines at SLAC, and is expected to be of further use in the determination of high-energy hadron source terms for shielding purposes, and in the estimation of induced radioactivity in targets, collimators, and beam dumps.

28.4   ACCELERATOR DESIGN APPLICATIONS

In the following sections, we will touch lightly on some recent applications of EGS4 to the design of accelerators, most notably the SLAC Linear Collider (SLC) (for a comprehensive introduction to the SLC itself, a recent paper by Fischer[31] should be of general interest). Most of the work described here has been reported elsewhere[32], and we will not go into much detail. Instead, we will simply emphasize some of the uses to which EGS has been put.
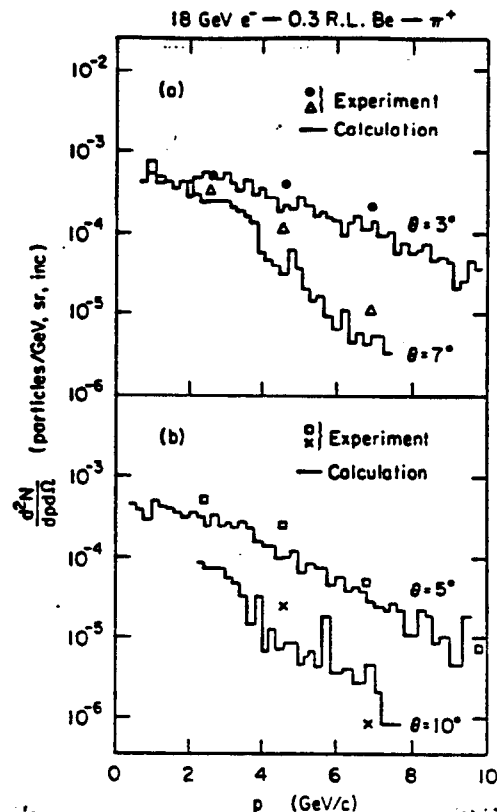
Figure 28.12. Comparison of π^+ yields from a $0.3X_0$ beryllium target hit by an 18-GeV electron beam.

28.4.1   Positron target design.

Secondary particle production is generally important around high-energy accelerator facilities, and the SLC at Stanford University is no exception. Indeed, successful operation of the SLC depends on the production of low-energy (2 to 20-MeV) positrons by 33-GeV electrons incident upon a positron production target.

The basic scheme behind the SLC project is to produce and collide a beam of 50-GeV positrons with a beam of 50-GeV electrons*, the purpose of which is to observe and measure intermediate vector bosons (Z^0, W^+, W^-) at the center-of-mass energy of 100 GeV. Production of low-energy positrons is accomplished by directing a 33-GeV electron beam into a high-Z target at the two-thirds point of the SLAC two-mile accelerator. These positrons are then "collected", re-injected into the machine, and accelerated, along with another beam of electrons, to the required energy of 50-GeV.

EGS4 was used in order to determine the size and nature of the target necessary to accomplish the task. As it turned out, a $6X_0$ high-Z target (90% Ta, 10% W) was selected on the basis that it produced enough positrons in the energy range of interest, as well as satisfying various engineering needs. Figure 28.13 shows an EGS4 shower generated by a single 33-GeV electron striking the $6X_0$ cylindrical target, where

---

* 5×10^{10} e^+ and e^-/pulse at 180 pulses/sec.

photons are shown as dots and charged particles as solid lines. Figure 28.14 is for the same statistical run, but this time only the positrons are shown.
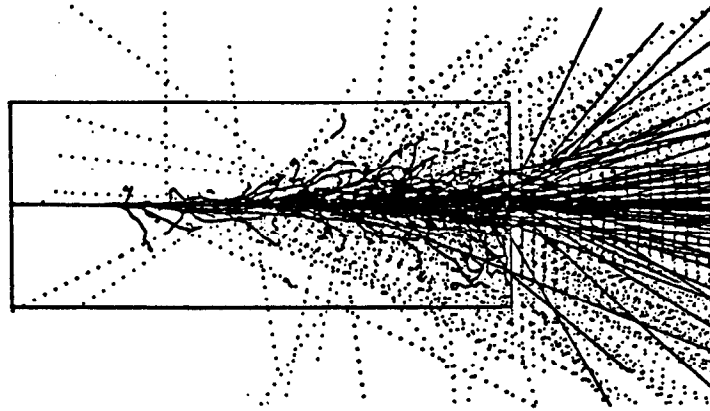

Figure 28.13. Shower produced in $6X_0$ cylindrical target struck by a single 33-GeV electron (all particles shown).
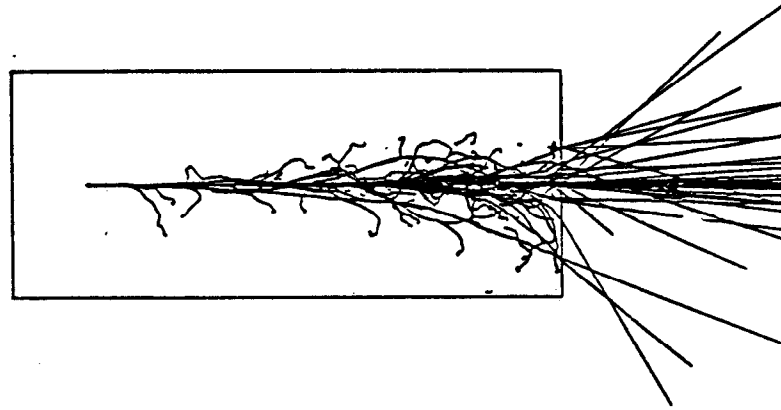

Figure 28.14. Shower produced in $6X_0$ cylindrical target struck by a single 33-GeV electron (positrons only shown).

Clearly, not only are a lot of positrons created by a single electron, but there is a central core of energy deposition that can lead to serious engineering problems, particularly target heating and melting. This core is primarily due to the production of bremsstrahlung followed by pair production. The small size of the core is determined by the characteristic angle of these processes—i.e., the ratio of the electron rest mass to the incident energy—convoluted with the charged particle multiple-scattering angle given above (Eqn. 28.10). The core dimension turns out to be very small at the high energies involved. Furthermore, the incident beam spot is Gaussian and of the order of 50 microns ($\sigma_x = \sigma_y = 50 \times 10^{-4}$ cm), so that even with a single pulse of 5×10^{10} e^-, the temperature rise is extremely high—i.e., in excess of 500°C/pulse (note: the melting temperature of the Ta-W target is 3035°C). The target wheel, inside a vacuum chamber, is rotated at 2 Hz to distribute the power from the beam operating at 180 pps, and the target is cooled by water passages in the drive shaft. The resulting stress from

each thermal pulse is $\approx 32,000$ psi, and the real concern involves a scenerio in which cracks develop due to material fatigue, leading to discontinuities in the heat transport path, and ultimately a melt down[33]. Therefore, EGS has been useful in determining not only the optimum positron yield, but also to point out some of the difficulties involved in running small beam spots into thick targets. In addition, since the positron target is a water-cooled device spinning in a vacuum, a number of components are made of materials that are subject to radiation damage, and EGS has been very useful in estimating their mean life to failure.

28.4.2 Heating of beam pipes and other components.

Although targets are usually cooled and the size of the beam spot can be purposely made larger to help alleviate problems, the same is not generally true of beam pipes, beam position monitors, and many other components. Under normal operations of the SLC, for example, both the positron and electron beams are designed to travel down the center of the beam pipe. EGS4 was used to forecast the difficulties that would arise should a beam inadvertantly impinge upon the pipe at a small grazing angle ($\sim$ few milliradians)[34]. Typically, we found temperature rises of 50 to 100°C/pulse for aluminum ($T_{melt} = 660°$C), and 300 to 700°C/pulse for copper ($T_{melt} = 1083°$C), depending upon the grazing angle. From these studies, it was determined that the temperature rise in copper precluded its use, and aluminum was chosen instead as the SLC beam pipe material.

Similarly, an EGS4 study was made to find out if the beam position monitors (BPMs), which are located outside the beam pipe radius, would suffer in any way due to shower leakage from beams inadvertantly striking the beam pipe upstream at a glancing angle—i.e., shower "punch through"[35]. The study showed that, for BPMs made out of stainless steel, the temperature rise could increase to the extent that they could lose their calibration. Obviously this was undesirable, so it was recommended that the BPMs be made out of aluminum instead.

28.4.3 Synchrotron radiation.

The spectral distribution of synchrotron radiation has adequately been described by many authors, starting from the original derivation by Schwinger[36]. In 1975, Nelson et al [37] pointed out that a large fraction of the synchrotron radiation associated with the PEP storage ring at SLAC would scatter out of the beam pipe and cause significant radiation damage to coil windings, plastic hoses, etc. In addition, the production of ozone in trapped layers could result in the creation of nitric acid, leading to further difficulties with the passage of time.

As an aid to understanding the overall problem, a series of EGS calculations have been performed over the years, not only for the PEP facility, but also for LEP at CERN[38], the SLC at SLAC[39], as well as other high-energy accelerator facilities[40]. Our intention is not to discuss any of the details involved in these problems at this time, but merely to point out that methods have been developed for sampling a synchrotron radiation spectrum for direct input into EGS. Of particular interest is an application* to the production of photoneutrons in the materials surrounding the beam pipe of LEP[38,41].

28.5   SIMULATION OF A HYDROGEN BUBBLE CHAMBER

In closing, we would like to illustrate the use of EGS4 for radiation transport in magnetic fields. To some extent, this has been described in the EGS4 manual[1] for a problem involving low-energy electrons. Reference is also made in the EGS4 manual to what has become an award-winning paper by Rawlinson, Bielajew, Galbraith, and Munro[42] in which EGS4 was also used to transport radiation in a strong electric field.

Recently, there has been a fair amount of interest at SLAC in using EGS4 to simulate the production and transport of background radiation in the large detectors associated with the SLC project. To provide an example of how one can accomplish this, an EGS4 User Code was created** to simulate a one-meter hydrogen bubble chamber. Figure 32.15 is a 1-GeV photon-initiated EM cascade in the SLAC 40-inch (one meter) LH_2 bubble chamber, consisting of an iron cylinder 2.5-cm thick containing liquid hydrogen, and with a $0.5X_0$ Pb slab at the center. The photon enters the chamber from the bottom where it strikes the plate at 90°. The magnetic field strength is 20 kGauss, and is applied along the cylinder axis. Bremsstrahlung is produced rather dramatically into the forward direction. One can easily identify the following interactions in this picture: bremsstrahlung, pair production, Compton scattering, both Bhabha and Møller delta rays, and ionization loss.

The same set of statistics are provided in Fig. 28.16, but this time only the charged particles are visible—which is what one sees in real bubble chamber pictures.

---

* The EGS4 User Code: UCGAMNSR.
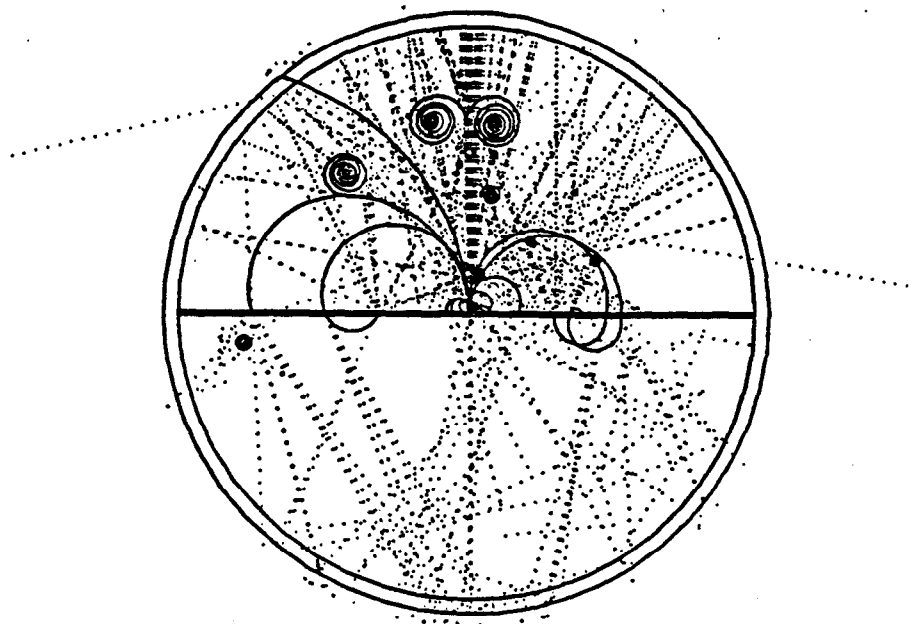** The EGS4 User Code: UPBUBBLE.

Figure 28.15. Hydrogen bubble chamber: A single 1-GeV photon strikes a $0.5X_0$ Pb slab from the bottom at $90°$. All charged particles (solid) and photons (dots) are shown.
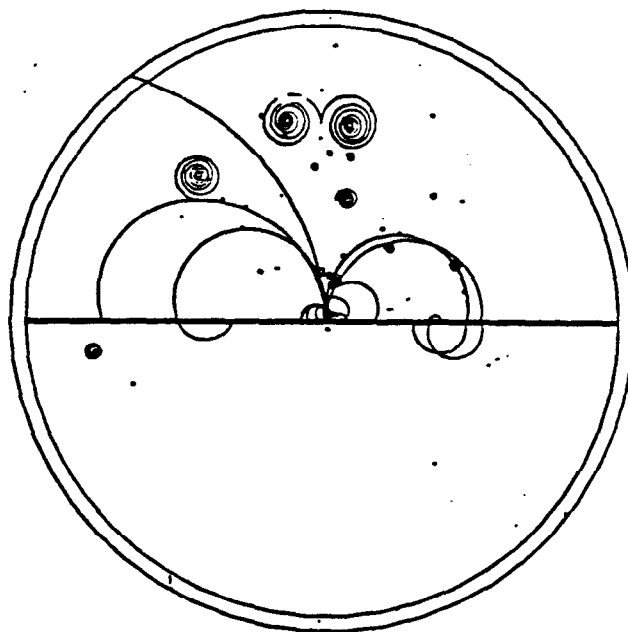

Figure 28.16. Hydrogen bubble chamber, but only charged particles (solid) are shown.

REFERENCES

1. W. R. Nelson, H. Hirayama and D. W. O. Rogers, "The EGS4 Code System", Stanford Linear Accelerator Center report SLAC-265 (1985).

2. Y. S. Tsai, "Pair Production and Bremsstrahlung of Charged Leptons", Rev. Mod. Phys. **46** (1974) 815.

3. D. F. Crawford and H. Messel, "Energy Distribution in Low-Energy Electron-Photon Showers in Lead Absorbers", Phys. Rev. **128** (1962) 2352.

4. H. H. Nagel, "Die Berechnung von Elektron-Photon-Kaskaden in Blei mit Hilfe der Monte-Carlo Methode", Inaugural-Dissertation zur Erlangung des Doktorgrades der Hohen Mathematich-Naturwissenschaftlichen Fakultät der Rheinischen Freidrich-Wilhelms-Universität zu Bonn, 1964; "Elektron-Photon-Kaskaden in Blei", Z. Phys. **186** (1965) 319.

5. U. Völkel, "Elektron-Photon-Kaskaden in Blei für Primärteilchen der Energie 6 GeV", DESY report DESY 65/6 (1965); "A Monte-Carlo Calculation of Cascade Showers in Copper Due to Primary Photons of 1 GeV, 3 GeV, and 6 GeV, and 6-GeV Bremsstrahlung Spectrum", DESY report DESY 67/16 (1967).

6. H. Messel and D. F. Crawford, *Electron-Photon Shower Distribution Function*, (Pergamon Press, Oxford, 1970).

7. R. L. Ford and W. R. Nelson, "The EGS Code System: Computer Programs for the Monte Carlo Simulation of Electromagnetic Cascade Showers (Version 3)", Stanford Linear Accelerator Center report SLAC-210 (1978).

8. S. Iwata, "Calorimeter", Nagoya University Department of Physics report DPNU-13-80 (1980).

9. J. Engler, "Perspectives in Calorimetry", Nucl. Instr. Meth. **235** (1985) 301.

10. P. Blüm, H. Guigas, H. Kock, M. Meyer, H. Poth, U. Raid, B. Richter, G. Backenstoss, M. Hasinoff, P. Pavlopoulos, J. Repond, L. Tauscher, D. Troster, L. Adiels, I. Bergstrom, K. Fransson, A. Kerek, M. Suffert and K. Zioutas, "A Modular NaI(Tℓ) Detector for 20-1000 MeV Photons", Nucl. Instr. Meth. **213** (1983) 251.

11. D. F. Anderson, G. Charpak, W. Kusmierz, P. Pavlopoulos and M. Suffert, "Test Results of a BaF$_2$ Calorimeter Shower with Wire Chamber Readout", Nucl. Instr. Meth. **228** (1984) 33.

12. U. Amaldi, "Fluctuations in Calorimetry Measurements", Physica Scripta **23** (1981) 409.

13. A. Abashian, J. Bjorken, C. Church, S. Ecklund, L. Mo, W. R. Nelson, T. Nunamaker, P. Rassman and D. Scherer, "Search for Neutral, Penetrating, Metastable Particles Produced in the SLAC Beam Dump", presented at the Fourth Moriond Workshop on Massive Neutrinos in Particle and Astrophysics, LaPlagne, France (15-21 January 1984).

14. A. J. Cook, "Mortran3 User's Guide", SLAC Computation Research Group technical memorandum CGTM 209 (1983).

15. H. Hirayama, W. R. Nelson, A. Del Guerra, T. Mulera and V. Perez-Mendez, "Monte Carlo Studies for the Design of a Lead-glass Drift Calorimeter", Nucl. Instr. Meth. **220** (1984) 327.

16. L. E. Price, "Drift-Collection Calorimeter", Physica Scripta **23** (1980) 685.

17. H. G. Fisher and O. Ullaland, "A High Density Projection Chamber", IEEE Trans. Nucl. Sci. **NS-27** (1980) 38.

18. T. Mulera and V. Perez-Mendez, "Observation of Large Saturated Pulses in Wire

Chambers Filled With Ar-CO$_2$ Mixtures", Nucl. Instr. Meth. **203** (1982) 609; (see references therein).

19. M. Conti, A. Del Guerra, R. Habel, T. Mulera, V. Perez-Mendez, G. Schwartz, "Use of a High Lead Glass Tubing Projection Chamber in Positron Emission Tomography and in High Energy Physics", Nucl. Instr. Meth., **A225** (1987) 207.

20. T. Mulera, V. Perez-Mendez, H. Hirayama, W. R. Nelson, R. Bellazzini, A. Del Guerra, M. M. Massai, "Drift Collection Calorimetry Using a Combined Radiator and Field Shaping Structure of Lead Glass Tubing", IEEE Trans. Nucl. Sci. **NS-31** (1984) 64.

21. D. Hitlin, J. F. Martin, C. C. Morehouse, G. S. Abrams, D. Briggs, W. Carithers, S. Cooper, R. Devoe, C. Friedberg, D. Marsh, S. Shannon, E. Vella and J. S. Whitaker, "Test of a Lead-Liquid Argon Electromagnetic Shower Detector", Nucl. Instr. Meth. **137** (1976) 225.

22. A. Del Guerra, M. Conti, G. Gorini, P. Lauriola, P. Maiano and C. Rizzo, "Energy Resolution Measurements of a Lead Glass Drift Calorimeter Prototype", presented at the IEEE Nuclear Science Symposium, San Francisco, 21-23 October 1987.

23. K. Kleinknecht, *Detectors for Particle Radiation*, (Cambridge University Press, Cambridge, 1986).

24. D. H. Perkins, *Introduction to High Energy Physics* (Addison-Wesley Publishing Co., Menlo Park, CA, 1987).

25. P. A. Aarnio, A. Fasso, H. J. Moehring, J. Ranft and G. R. Stevenson, "FLUKA86 User's Guide", CERN Divisional report TIS-RP/168 (1986).

26. P. A. Aarnio, J. Lindgren, J. Ranft, A. Fasso and G. R. Stevenson, "Enhancements to the FLUKA86 Program (FLUKA87)", CERN Divisional report TIS-RP/190 (1987).

27. J. Ranft, H. J. Möhring, T. M. Jenkins and W. R. Nelson, "The Hadron Cascade Code FLUKA82: Setup and Coupling with EGS4 at SLAC", Stanford Linear Accelerator Center report SLAC-TN-86-3 (1986).

28. K. C. Chandler and T. W. Armstrong, "Operating Instructions for the High-Energy Nucleon-Meson Transport Code, HETC", Oak Ridge National Laboratory report ORNL-4744 (1972).

29. F. S. Alsmiller, T. A. Gabriel, R. G. Alsmiller, "Hadron-Lepton Cascade Calculations (1-20 GeV) for a Pb-Al-Lucite Calorimeter", Oak Ridge National Laboratory report ORNL/TM-9153 (1984).

30. J. Ranft and W. R. Nelson, "Hadron Cascades Induced by Electron and Photon Beams in the GeV Energy Range", Nucl. Instr. Meth. **A257** (1987) 177.

31. G. E. Fischer (for the SLAC Staff), "SLC—Status and Development", Stanford Linear Accelerator Center report SLAC-PUB-4012 (1986).

32. T. M. Jenkins and W. R. Nelson, "Unique Radiation Problems Associated with the SLAC Linear Collider", Stanford Linear Accelerator Center report SLAC-PUB-4179 (1986); CONF 8602106, Invited talk at the Midyear Symposium of the Health Physics Society (Reno, Nevada, February 8-12, 1987).

33. S. Ecklund and W. R. Nelson, "Energy Deposition and Thermal Heating in Materials Due to Low Emittance Electron Beams", Stanford Linear Accelerator Center collider note CN-135 (1981).

34. W. R. Nelson and T. M. Jenkins, "Temperature Rise Calculations for the Beam Pipe in the SLC Arcs", Stanford Linear Accelerator Center collider note CN-235 (1983).

35. W. R. Nelson and T. M. Jenkins, "Temperature Rise in Iron Beam Position Monitors", Stanford Linear Accelerator Center collider note CN-276 (1984).

36. J. Schwinger, "On the Classical Radiation of Accelerated Electrons", Phys. Rev. 75 (1949) 1912.

37. W. R. Nelson, G. J. Warren and R. L. Ford, "The Radiation Dose to the Coil Windings and the Production of Nitric Acid and Ozone from PEP Synchrotron Radiation", Stanford Linear Accelerator Center PEP note PEP-109 (1975).

38. W. R. Nelson and J. W. N. Tuyn, "Neutron Production by LEP Synchrotron Radiation Using EGS", CERN internal report CERN-HS-RP/037 (1979); also distributed as LEP Note 187 (1979).

39. T. M. Jenkins and W. R. Nelson, "Synchrotron Radiation in the Collider Arcs", Stanford Linear Accelerator Center collider note CN-69 (1981).

40. C. Yamaguchi, "Absorbed Dose and Energy Deposition Calculation Due to Synchrotron Radiation from PETRA, HERA and LEP", DESY Internal report DESY D3/38 (1981).

41. T. M. Jenkins and M. Hofert, "The Effects of Synchrotron Radiation from the Wigglers", CERN internal report CERN-TIS-RP/IR/85-23 (1985).

42. J. A. Rawlinson, A. F. Bielajew, D. M. Galbraith and P. Munro, "Theoretical and Experimental Investigation of Dose Enhancement Due to Charge Storage in Electron-Irradiated Phantoms", Med. Phys. 11 (1984) 814.